

# Inertial Magnetic SLAM Systems Using Low-Cost Sensors

Chuan Huang, Graduate Student Member, IEEE, Gustaf Hendeby, Senior Member, IEEE,  
and Isaac Skog, Senior Member, IEEE

**Abstract**— Spatially inhomogeneous magnetic fields offer a valuable, non-visual information source for positioning. Among systems leveraging this, magnetic field-based simultaneous localization and mapping (SLAM) systems are particularly attractive because they can provide positioning information and build a magnetic field map on the fly. Moreover, they have bounded error within mapped regions. However, state-of-the-art methods typically require low-drift odometry data provided by visual odometry or a wheel encoder, etc. This is because these systems need to minimize/reduce positioning errors while exploring, which happens when they are in unmapped regions. To address these limitations, this work proposes a loosely coupled and a tightly coupled inertial magnetic SLAM (IM-SLAM) system. The proposed systems use commonly available low-cost sensors: an inertial measurement unit (IMU), a magnetometer array, and a barometer. The use of non-visual data provides a significant advantage over visual-based systems, making it robust to low-visibility conditions. Both systems employ state-space representations, and magnetic field models on different scales. The difference lies in how they use a local and global magnetic field model. The loosely coupled system uses these models separately in two state-space models, while the tightly coupled system integrates them into one state-space model. Experiment results show that the tightly coupled IM-SLAM system achieves lower positioning errors than the loosely coupled system in most scenarios, with typical errors on the order of meters per 100 meters traveled. These results demonstrate the feasibility of developing a full 3D IM-SLAM systems using low-cost sensors and the potential of applying these systems in emergency response scenarios such as mine/fire rescue.

**Index Terms**— inertial navigation, SLAM, indoor positioning, magnetic field, low-cost sensors.

## I. INTRODUCTION

POSITIONING and navigation services are essential for various applications, including scientific research, emergency response, and military operations. These services have historically relied on the global navigation satellite system (GNSS). However, GNSS-denied environments,

This work has been funded by the Swedish Research Council (Vetenskapsrådet) project 2020-04253 "Tensor-field based localization".

Chuan Huang is with the Dept. of Electrical Engineering and Computer Science, KTH Royal Institute of Technology, Stockholm, Sweden (e-mail: chuanh@kth.se).

Gustaf Hendeby is with the Dept. of Electrical Engineering, Linköping University (e-mail: gustaf.hendeby@liu.se).

Isaac Skog is with the Dept. of Electrical Engineering and Computer Science, KTH Royal Institute of Technology, 10044 Stockholm, Sweden, and also with the Division of Underwater Technology, Swedish Defence Research Agency (FOI), Kista, Sweden (e-mail: skog@kth.se).

such as deep sea, indoor environments, and battlefields, where GNSS signals are unavailable or unreliable, pose significant challenges for accurate and reliable positioning. Therefore, developing robust and precise positioning systems that can operate effectively in GNSS-denied environments is of paramount importance.

A common approach to address the challenges in positioning in GNSS-denied environments is to use additional sensors, such as cameras, Light Detection and Ranging (LiDAR) sensors, and inertial measurement units (IMUs), to complement the GNSS. For example, visual and LiDAR Simultaneous localization and mapping (SLAM) systems [1], [2] have been widely used for indoor positioning. However, these systems have their own limitations. Visual SLAM systems are sensitive to lighting conditions and may fail in low-light or featureless environments [3], and LiDAR SLAM systems can be expensive and may function poorly in environments with limited geometric features [4]. Thus, it is necessary to exploit other types of environmental features to achieve robust indoor SLAM.

Indoor magnetic fields have been recognized as a promising source of environmental features for SLAM [5]. Because of the ubiquitous presence of ferromagnetic materials in buildings, the indoor magnetic field exhibits spatial variations, which can be used as location fingerprints. As is shown in Fig. 1, the magnetic field strength inside a building can vary significantly over short distances, making it a useful feature for SLAM applications. Moreover, magnetic field measurements can be obtained using low-cost magnetometers, which are commonly found in smartphones and other portable devices. This makes magnetic field SLAM systems cost-effective and accessible.

Previous works have shown that magnetic field SLAM systems can achieve meter-level accuracy in indoor environments [6]–[10]. However, most of these systems rely on low-drift odometry data, such as that from wheel odometry or visual odometry, to provide motion constraints, or they assume planar 2D motion, which limits their availability and applicability in real-world scenarios. Furthermore, these systems use a single magnetometer, which makes SLAM more challenging because a measurement of the magnetic field at a single point provides limited information about the spatial variations in the magnetic field. To address these issues, in a recent work [11], a magnetic field-aided inertial navigation system was developed. This system uses a low-cost IMU and a magnetometer array

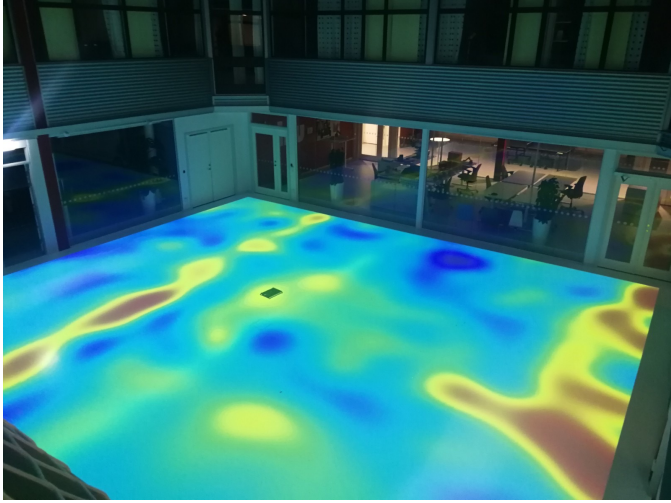


**Fig. 1.** Illustration of the magnetic-field magnitude variations, represented by different colors, near the floor in a room of **12 × 12** square meters.

consisting of 30 magnetometers, which allows snapshots of magnetic field over a planar sensor board to be taken. This system can provide low-drift inertial navigation that has the potential to be used, instead of wheel odometry or visual odometry, in a magnetic-field SLAM system. Inspired by this work, we seek to answer the following research questions:

- Can a 3D inertial magnetic SLAM (IM-SLAM) system be built and provide meter-level positioning using only a low-cost IMU, barometer, and magnetometer array?
- What is a suitable sensor fusion strategy? How does the performance of a tightly-coupled IM-SLAM system compare to a loosely-coupled IM-SLAM systems?
- How does the barometer and the quality of the inertial sensor measurements affect the overall performance of the SLAM system?

To that end, we propose two IM-SLAM systems: a loosely coupled and a tightly coupled system. Different from previous magnetic field SLAM systems, the proposed systems do not require odometric information from visual or wheel-encoder sensors. This makes the systems much more adaptable to various environments where traditional odometry might fail.

## A. Related Work

Many methods for magnetic field-based indoor positioning and navigation have been proposed. They are generally classified into two categories: infrastructure-based methods [12] and infrastructure-free methods [13], [14]. The former generally requires some magnetic source to be installed in the environment, such as magnetic coils or magnets. The latter, on the other hand, exploits the ambient magnetic field as a location fingerprint. The infrastructure-free methods are more appealing because they are easier to deploy and maintain. Therefore, our focus is on the infrastructure-free methods.

The infrastructure-free methods can be further classified into two categories: fingerprinting-based methods [14]–[19] and model-based methods [6], [7], [10], [11], [13], [20]–[22]. The fingerprinting-based methods are based upon the assumption that the magnetic fields at different locations are distinct. These methods generally rely on matching real-time magnetic field measurements to a pre-established magnetic field map to estimate location, or to a stored measurement history to recognize previously visited locations for loop closure. The model-based methods, on the other hand, seek to use a mathematical model to describe magnetic fields measurements. These methods can use the magnetic measurements to update their magnetic field model (build a magnetic field map) and estimate pose change as the device moves through the environment. There are pros and cons for both methods. The fingerprinting-based methods can achieve high accuracy if magnetic field matching is successful, but they require carefully designed feature extraction and matching algorithms. Furthermore, erroneous matching can lead to significant localization errors. In contrast, the model-based methods are easier to analyze from a theoretical perspective, but they can be sensitive to the choice of the magnetic field model and the tuning of the model parameters.

The proposed IM-SLAM systems are model-based. They were made possible by the development in magnetic field odometry and previous works on magnetic field modeling. In [20], a polynomial model was proposed to locally approximate the magnetic field, which was later extended in [21] to estimate pose changes of a magnetometer array between two time instants. The very same polynomial model was also used in [11] to build a magnetic field aided inertial navigation system (MAINS), which effectively reduced the positioning drift of the inertial navigation system by 2 orders of magnitude. This work constitutes one of the building blocks of the proposed SLAM systems. The other building block comes from the work in global magnetic field modeling. Originally proposed in [23], the reduced rank Gaussian process (GP) model was shown to be effective and computationally efficient in modeling the indoor magnetic field on a global scale. The GP model was later used in [6], [7], [24] to build magnetic field SLAM systems.

## B. Contributions

The contributions of this work are as follows:

- A loosely-coupled and tightly-coupled IM-SLAM systems using low-cost sensors are proposed.
- An extensive evaluation is conducted on real-world datasets, encompassing challenging indoor environments with multi-floor structures.
- The implementation of the proposed systems and the datasets used for evaluation are made publicly available to provide a reproducible benchmark.

Reproducible research: Both the datasets and algorithms used in this study are available at <https://github.com/Huang-Chuan/IM-SLAM>.

## II. PRELIMINARIES

As magnetic field modeling is essential for magnetic field SLAM, we briefly review two commonly used magnetic field models in this section; the first model is for modeling the magnetic field at local small scales, and the second is at global large scales.

Let us start with magnetostatics. Assuming that there is no time-varying electric field and current density in the region of interest, the magnetic field fulfills the curl-free condition [25, p. 180]

$$\nabla \times M(r) = 0 \quad (1)$$

where  $r \in \mathbb{R}^3$  denotes the position in the Cartesian coordinates. This permits the expression of  $M(r)$  as the gradient of a scalar potential function  $\phi(r) : \mathbb{R}^3 \rightarrow \mathbb{R}$ , i.e.,

$$M(r) = \nabla \phi(r). \quad (2)$$

Both of the two magnetic field models presented next are based on (2).

### A. Local Magnetic Field Model

A local magnetic field model refers to a model that captures the magnetic field in a small region of space where the field can be well approximated by a simple function. The polynomial model proposed in [20] is a model of this type. It provides a compact local representation of the magnetic field. In this model, the scalar potential function is assumed to be an  $(n+1)$ -degree polynomial function, i.e.,

$$\phi(r; c) = \sum_{\substack{i,j,k \geq 0 \\ i+j+k \leq n+1}} c_{i,j,k} r_x^i r_y^j r_z^k. \quad (3)$$

Here  $c_{i,j,k} \in \mathbb{R}$  denotes the coefficient and  $r \triangleq [r_x \ r_y \ r_z]^\top$ . Furthermore, the coefficients of the resulting magnetic field model  $M(r; c)$  from applying (2) are further constrained by the divergence-free condition [25, p. 180]

$$\nabla \cdot M(r; c) = 0. \quad (4)$$

It leads to a  $n$ -th degree polynomial magnetic field model [20]

$$M(r; \theta) = \Phi(r) \theta \quad (5)$$

where  $\Phi(r) \in \mathbb{R}^{3 \times p}$  denotes the regressor matrix,  $\theta \in \mathbb{R}^{p \times 1}$  denotes the coefficients, with  $p = n^2 + 4n + 3$ .

It has been empirically verified in [11] that a first-degree polynomial magnetic field model can capture indoor magnetic fields on a planar magnetometer array of size 345 mm  $\times$  245 mm. The regressor matrix in this case is

$$\Phi(r) = \begin{bmatrix} 1 & 0 & 0 & 0 & 0 & r_z & r_y & 2r_x \\ 0 & 1 & 0 & r_z & 2r_y & 0 & r_x & 0 \\ 0 & 0 & 1 & r_y & -2r_z & r_x & 0 & -2r_z \end{bmatrix} \quad (6a)$$

and

$$\theta = [\theta(1) \ \theta(2) \ \dots \ \theta(8)]^\top. \quad (6b)$$

### B. Global Magnetic Field Model

A global magnetic field model refers to a model that describes the magnetic field across the entire environment, such as a building or a large lab. The approximated GP model proposed in [23] allows for efficient regression with much less computational complexity than the full GP model. The development of the magnetic field model starts with modeling the scalar magnetic potential function  $\phi(r)$  as a GP

$$\phi(r) \sim \mathcal{GP}(0, \kappa_{\text{lin.}}(r, r') + \kappa_{\text{SE}}(r, r')) \quad (7a)$$

where

$$\kappa_{\text{lin.}}(r, r') = \sigma_{\text{lin.}}^2 r^\top r' \quad (7b)$$

and

$$\kappa_{\text{SE}}(r, r') = \sigma_{\text{SE}}^2 \exp\left(-\frac{\|r - r'\|^2}{2l_{\text{SE}}^2}\right). \quad (7c)$$

Here  $\sigma_{\text{lin.}}$  denotes the magnitude scale of the linear kernel  $\kappa_{\text{lin.}}$ ,  $\sigma_{\text{SE}}$  and  $l_{\text{SE}}$  denote the magnitude scale and the characteristic length scale of the square exponential kernel  $\kappa_{\text{SE}}$ , respectively. To reduce the computation complexity, the square exponential kernel is approximated by

$$\kappa_{\text{SE}}(r, r') \approx \sum_{j=1}^m S_{\text{SE}}(\lambda_j) \psi_j(r) \psi_j(r') \quad (8a)$$

where  $m$  is the number of basic functions and  $S_{\text{SE}}(\cdot)$  denotes the spectral density of  $\kappa_{\text{SE}}$ . Furthermore,  $\psi_j(\cdot)$  and  $\lambda_j$  denote the  $j$ -th eigenfunction and eigenvalue of the Laplace operator in the domain of a cuboid  $([-L_x, L_x] \times [-L_y, L_y] \times [-L_z, L_z])$  with Dirichlet boundary conditions, respectively. They are given by

$$\psi_j(r) = \prod_{d=x,y,z} \frac{1}{\sqrt{L_d}} \sin\left(\frac{\pi n_{j,d}(r_d + L_d)}{2L_d}\right) \quad (8b)$$

$$\lambda_j^2 = \sum_{d=x,y,z} \left(\frac{\pi n_{j,d}}{2L_d}\right)^2 \quad (8c)$$

respectively, where  $n_{j,d} \in \mathbb{Z}^+$ . Combining (7a) and (8a) and relating to the weight space view [26, Ch. 2], the scalar potential function is then approximated by

$$\phi(r; \eta) \approx \Psi(r) \eta, \quad \eta \in \mathbb{R}^{3+m} \quad (9a)$$

where

$$\Psi(r) = [r^\top \ \psi_1(r) \ \psi_2(r) \ \dots \ \psi_m(r)] \quad (9b)$$

$$\eta \sim \mathcal{N}(0, \Lambda) \quad (9c)$$

and

$$\Lambda = \text{diag}(\sigma_{\text{lin.}}^2, \sigma_{\text{lin.}}^2, \sigma_{\text{lin.}}^2, S_{\text{SE}}(\lambda_1), S_{\text{SE}}(\lambda_2), \dots, S_{\text{SE}}(\lambda_m)). \quad (9d)$$

Here  $\mathcal{N}(0, \Lambda)$  denotes a Gaussian distributed random variable with mean 0 and covariance matrix  $\Lambda$ . The global magnetic field model is obtained by applying (2) to the approximated scalar potential function, i.e.,

$$M(r; \eta) = \nabla \phi(r; \eta) \approx \nabla \Psi(r) \eta. \quad (10)$$

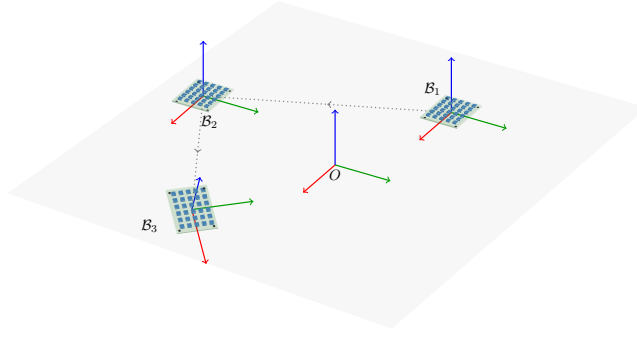


Fig. 2. Coordinate frames used by the local and global magnetic field models. The local magnetic field model at each time step aligns with the body frame of the magnetometer array, e.g.,  $\mathcal{B}_1, \mathcal{B}_2$  and  $\mathcal{B}_3$ , while the global magnetic field model uses the navigation frame denoted by  $O$  in the middle of the plot.

### C. Discussion

The polynomial model presented in Section II-A is well-suited for local modeling, due to its simplicity and efficiency. The first-degree polynomial model was used in [11] to model the magnetic field within the small area covered by the magnetometer array at each time step (see Fig. 2). In this model, both the spatial coordinates and the magnetic field are expressed in the body frame of the magnetometer array.

On the other hand, the approximated GP model presented in Section II-B is more appropriate for global modeling, as the sinusoidal basis functions can capture the magnetic field variations across a larger area. It is more computationally demanding than the first-degree polynomial model. Typically, several hundreds to thousands of basis functions are used to represent the magnetic field across an area of several hundred square meters [7]. Since this model aims to describe the field over a global region, both the spatial coordinates and the magnetic field are expressed in the navigation frame.

## III. MAGNETIC FIELD-BASED POSITIONING SYSTEMS

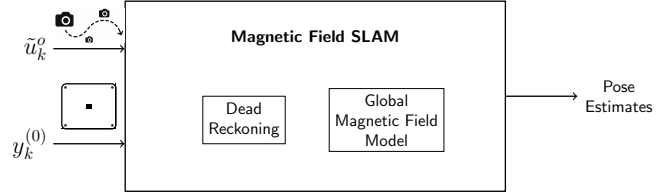
In this section, we briefly review the system models in two magnetic field-based positioning systems: the first is the magnetic field SLAM system proposed in [7], and the second is the MAINS proposed in [11]. These systems, illustrated in Fig. 3a and Fig. 3b, are the foundations of the proposed IM-SLAM systems.

### A. The Magnetic Field SLAM System

The state-of-the-art magnetic field SLAM system [7] uses low-drift visual odometry and magnetic field measurements from a single magnetometer. The basic idea is to perform dead-reckoning using the visual odometry data and use magnetic field measurements to correct the accumulated position drift.

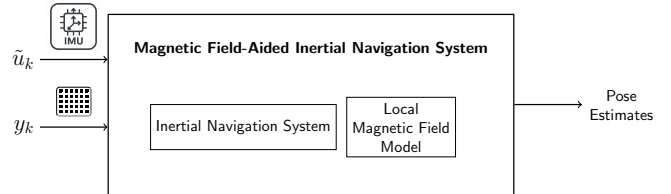
The state vector of the magnetic field SLAM at time step  $k$  is defined as

$$x_k^{\text{SLAM}} \triangleq [p_k^\top \ q_k^\top \ \eta_k^\top]^\top \quad (11)$$



$\tilde{u}_k^o$ : visual odometry data  
 $y_k^{(0)}$ : a single magnetometer's measurements

(a)



$\tilde{u}_k$ : IMU measurements  
 $y_k$ : magnetometer array measurements

(b)

Fig. 3. (a) An overview of the magnetic field SLAM system [7]. The system performs dead reckoning using visual odometry data and uses a global magnetic field model to register a single magnetometer's measurements, which are used to correct position drift. (b) An overview of the MAINS. The system performs inertial navigation using IMU measurements and uses a local magnetic field model to register a magnetometer array's measurements, which are used to correct velocity estimates.

where  $p_k \in \mathbb{R}^3$  denotes the position,  $q_k \in S^3$  denotes the orientation in quaternion representation, and  $\eta_k \in \mathbb{R}^{3+m}$  denotes the coefficients of the approximated GP magnetic field model.

The system model of the magnetic field SLAM is

$$x_{k+1}^{\text{SLAM}} = f^{\text{SLAM}}(x_k^{\text{SLAM}}, \tilde{u}_k^o) \quad (12a)$$

$$y_k^{(0)} = h^{\text{SLAM}}(x_k^{\text{SLAM}}) + e_k^{(0)} \quad (12b)$$

where

$$f^{\text{SLAM}}(x_k^{\text{SLAM}}, \tilde{u}_k^o) = \begin{bmatrix} p_k + \Delta p_k \\ q_k \otimes \Delta q_k \\ \eta_k \end{bmatrix} \quad (12c)$$

and

$$h^{\text{SLAM}}(x_k^{\text{SLAM}}) = R_k^\top \nabla \Psi(p_k) \eta_k. \quad (12d)$$

Here  $\tilde{u}_k^o = [\Delta p_k^\top \ \Delta q_k^\top]^\top$  denotes the visual odometry data, where  $\Delta p_k \in \mathbb{R}^3$  and  $\Delta q_k \in S^3$  denote the change in position and orientation, respectively. Furthermore,  $y_k^{(0)} \in \mathbb{R}^3$  and  $e_k^{(0)} \in \mathbb{R}^3$  are the magnetometer measurements and the Gaussian white measurement noise, respectively. In addition,  $\otimes$  denotes quaternion multiplication, and  $R_k \in SO(3)$  denotes the rotation matrix corresponding to the quaternion  $q_k$ .

### B. The Magnetic Field-Aided Inertial Navigation System

The MAINS proposed in [11] uses a low-cost IMU and magnetometer array (see Fig. 4) to provide low-drift inertial navigation. The basic idea is to use inertial

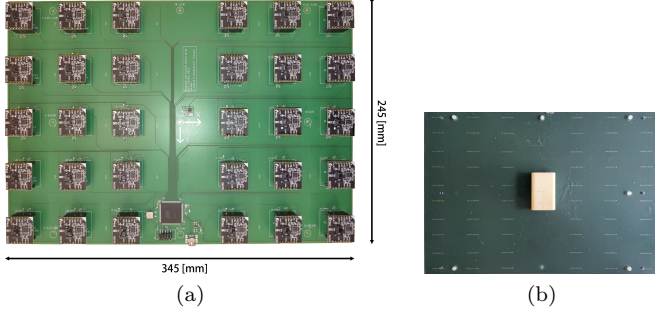


**Fig. 4.** The sensor board used in the magnetic field-aided inertial navigation system. It has 30 PNI RM3100 magnetometers and an Osmium MIMU 4844 IMU mounted on the bottom side. (a) Front side of the sensor board showing the magnetometer array. (b) Back side of the sensor board showing the IMU.

navigation system (INS) to estimate poses, and magnetic field measurements to correct velocity estimates.

The state vector of MAINS at time step  $k$  is defined as

$$x_k^{\text{mains}} \triangleq [x_k^{\text{ins}} \top \theta_k \top]^\top \quad (13a)$$

$$x_k^{\text{ins}} \triangleq [p_k \top v_k \top q_k \top b_{a,k} \top b_{g,k} \top]^\top \quad (13b)$$

where  $x_k^{\text{ins}}$  denotes the inertial navigation states. Furthermore,  $v_k \in \mathbb{R}^3$  denotes the velocity,  $b_{a,k} \in \mathbb{R}^3$  and  $b_{g,k} \in \mathbb{R}^3$  denote the accelerometer and gyroscope biases, respectively, and  $\theta_k \in \mathbb{R}^8$  denotes the coefficients of the first degree polynomial magnetic field model in Section II-A. The dynamics of the state vector and the measurement model are

$$x_{k+1}^{\text{mains}} = f^{\text{mains}}(x_k^{\text{mains}}, \tilde{u}_k, w_k) \quad (14a)$$

$$y_k = H^{\text{mains}} x_k^{\text{mains}} + e_k \quad (14b)$$

where

$$f^{\text{mains}}(x_k^{\text{mains}}, \tilde{u}_k, w_k) = \begin{bmatrix} f^{\text{ins}}(x_k^{\text{ins}}, \tilde{u}_k, w_k^{\text{ins}}) \\ f^\theta(\theta_k, x_k^{\text{ins}}, \tilde{u}_k, w_k^\theta) \end{bmatrix} \quad (14c)$$

and

$$H^{\text{mains}} = \begin{bmatrix} 0_{3 \times 16} & \Phi(r^{(1)}) \\ \vdots & \vdots \\ 0_{3 \times 16} & \Phi(r^{(N)}) \end{bmatrix}. \quad (14d)$$

Here  $f^{\text{ins}}(\cdot)$  denotes the inertial subsystem dynamics,  $f^\theta(\cdot)$  denotes the magnetic subsystem function. The exact form of these functions is presented in [11]. Moreover,  $\tilde{u}_k = [\tilde{a}_k \top \tilde{\omega}_k \top]^\top$  denotes the IMU measurements, where  $\tilde{a}_k \in \mathbb{R}^3$  and  $\tilde{\omega}_k \in \mathbb{R}^3$  denote the specific force and angular velocity, respectively. Furthermore,  $w_k = [(w_k^{\text{ins}})^\top (w_k^\theta)^\top]^\top$  denotes the process noise, where  $w_k^{\text{ins}} \in \mathbb{R}^{12}$  and  $w_k^\theta \in \mathbb{R}^8$  denote the process noise of the inertial and magnetic subsystems, respectively. The measurement vector  $y_k \in \mathbb{R}^{3N}$  denotes the magnetometer measurements from an array of  $N$  magnetometers, where  $r^{(i)}$  denotes the position of the  $i$ -th magnetometer in the array expressed in the body frame.  $\Phi(\cdot)$  denotes the regressor matrix in (6a). Finally,  $e_k \in \mathbb{R}^{3N}$  denotes the white Gaussian measurement noise.

### Loosely-Coupled Inertial Magnetic SLAM System

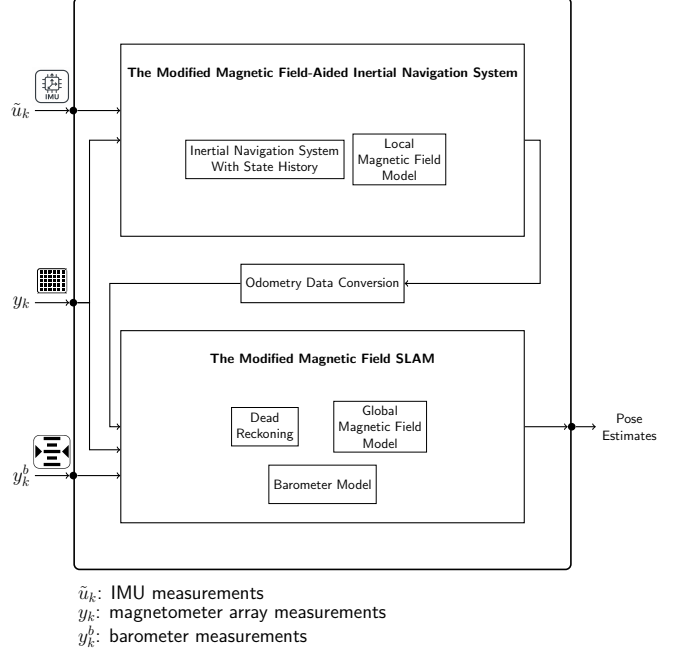


**Fig. 5.** An overview of the loosely-coupled IM-SLAM system. The system is a cascade of a modified MAINS, an odometry data conversion module, and a modified magnetic field SLAM system.

### C. Summary

Both the magnetic field SLAM system and the MAINS have their own advantages and limitations. The magnetic field SLAM system has a bounded positioning error in mapped regions. However, its reliance on the low-drift visual odometry limits its usability. The MAINS, on the other hand, can provide low-drift inertial navigation, but it only maintains a local magnetic field map and, thus, cannot provide positioning with bounded error. In the next section, we propose a loosely-coupled magnetic field SLAM system that combines the advantages of both systems while mitigating their limitations.

## IV. THE LOOSELY-COUPLED IM-SLAM SYSTEM

A loosely coupled IM-SLAM system can be regarded as a cascaded architecture composed of a modified MAINS and a modified magnetic field SLAM system, as illustrated in Fig. 5. The dependence on low-drift visual odometry data is eliminated by replacing it with odometry provided by the modified MAINS system. Furthermore, the measurement model in the magnetic field SLAM system is adapted to support magnetometer arrays, rather than a single magnetometer, as well as an additional barometer. The barometer supplies altitude information, enabling the SLAM system to achieve improved 3D trajectory estimation.

### A. Computing Odometry Data with the MAINS

The original MAINS [11] estimates the pose at the current timestep; therefore, it cannot be used directly to

compute odometry data. One way to make the MAINS support odometry data computation is to augment the state vector of MAINS to include the complete state vector (or the pose) at the past and compute the difference between the pose at the past and the current. A detailed explanation of this modification is presented next. The augmented state vector is defined as

$$x_k^a \triangleq [x_k^{\text{mains}\top} \ x_k^{\text{past}\top}]^\top \quad (15a)$$

$$x_1^{\text{past}} \triangleq x_1^{\text{mains}} \quad (15b)$$

$$x_k^{\text{past}} \triangleq f^{\text{past}}(x_{k-1}^{\text{past}}, x_{k-1}^{\text{mains}}), \quad k \geq 2 \quad (15c)$$

$$f^{\text{past}}(x_{k-1}^{\text{past}}, x_{k-1}^{\text{mains}}) = \begin{cases} x_{k-1}^{\text{past}} & nK + 3 \leq k \leq (n+1)K + 1 \\ x_{k-1}^{\text{mains}} & k = nK + 2 \end{cases} \quad (15d)$$

$$n = 0, 1, 2, \dots \quad (15e)$$

Here  $K \in \mathbb{N}$  denotes the number of time steps within the time interval for which the odometry data is computed. The state-space model of the modified MAINS is then

$$x_{k+1}^a = f^a(x_k^a, \tilde{u}_k, w_k) = \begin{bmatrix} f^{\text{mains}}(x_k^{\text{mains}}, \tilde{u}_k, w_k) \\ f^{\text{past}}(x_{k-1}^{\text{past}}, x_{k-1}^{\text{mains}}) \end{bmatrix} \quad (16a)$$

$$y_k = H^a x_k^a + e_k \quad (16b)$$

$$H^a = \begin{bmatrix} 0_{3 \times 16} & \Phi(r^{(1)}) & 0_{3 \times 16} \\ \vdots & \vdots & \vdots \\ 0_{3 \times 16} & \Phi(r^{(N)}) & 0_{3 \times 16} \end{bmatrix}. \quad (16c)$$

The modified MAINS can compute odometric data between the time step  $i = nK + 1$  and  $j = (n+1)K + 1$  using the posterior state estimate at time step  $j$  as

$$\tilde{u}_{i,j}^o = \begin{bmatrix} \Delta p_{i,j} \\ \Delta q_{i,j} \end{bmatrix} = \begin{bmatrix} \hat{p}_j - \hat{p}_i \\ \hat{q}_i^* \otimes \hat{q}_j \end{bmatrix} \quad (17a)$$

where  $(\hat{\cdot})_i$  and  $(\hat{\cdot})_j$  denote the smoothed and filtered quantity at time  $i$  and  $j$ , respectively, and  $(\cdot)^*$  denotes conjugated quaternion. The covariance of the odometry data can be approximated by

$$\text{Cov}(\tilde{u}_{i,j}^o) \approx A_{i,j} \text{Cov}(\hat{p}_i, \hat{p}_j, \hat{q}_i, \hat{q}_j) A_{i,j}^\top \quad (17b)$$

$$A_{i,j} = \begin{bmatrix} I_3 & -I_3 & 0_3 & 0_3 \\ 0_3 & 0_3 & I_3 & -\hat{R}_i^\top \hat{R}_j \end{bmatrix} \quad (17c)$$

where  $\text{Cov}(\cdot)$  denotes the covariance. Note the covariance of the quaternion is defined in the tangent space of  $S^3$ , see [27, p. 54] for details.

## B. The Modified Magnetic Field SLAM System

The modified magnetic field SLAM system uses the odometric data provided by the modified MAINS, magnetic field measurements from the sensor array, and barometer measurements. The state vector of this system and the dynamics remain the same as in Section III-A. The measurement equation is modified to

$$y_k = h^{\text{array-slam}}(x_k^{\text{SLAM}}) + e_k \quad (18a)$$

where

$$h^{\text{array-slam}}(x_k^{\text{SLAM}}) = \begin{bmatrix} R_k^\top \nabla \Psi(p_k + R_k r^{(1)}) \\ R_k^\top \nabla \Psi(p_k + R_k r^{(2)}) \\ \vdots \\ R_k^\top \nabla \Psi(p_k + R_k r^{(N)}) \end{bmatrix} \eta_k. \quad (18b)$$

Here  $h^{\text{array-slam}}(\cdot)$  denotes the modified measurement function, which takes into account the multiple sensors and the geometric configuration of the sensor array. This measurement equation is augmented when barometric measurements are available, i.e.,

$$y_k^b = p_{z,k} + e_k^b \quad (19)$$

where  $p_{z,k} \in \mathbb{R}$  denotes the altitude (the third component of the position vector), and  $e_k^b \in \mathbb{R}$  denotes the barometer measurement noise, modeled as Gaussian white noise.

## C. Summary

The loosely-coupled IM-SLAM system combines the advantages of both the magnetic field SLAM system and the MAINS. It is a self-contained system that can provide bounded-error positioning in mapped areas without the need for external low-drift odometry. However, there are two main limitations of this system. First, the magnetometer measurements are used twice: first in the modified MAINS and then in the modified magnetic field SLAM system. Second, the odometric data provided by the modified MAINS is correlated over time, which violates the assumption of uncorrelated odometric data in the magnetic field SLAM system. These two limitations can potentially degrade the performance of the loosely-coupled IM-SLAM system. To address these limitations, we propose a tightly-coupled IM-SLAM system in the next section.

## V. THE TIGHTLY-COUPLED IM-SLAM SYSTEM

The tightly-coupled IM-SLAM system integrates the inertial, barometric, and magnetic sensors into a unified SLAM framework (see Fig. 6). In this framework, the state vector encompasses the full set of states, including the inertial states, local and global magnetic field model coefficients. The system dynamics and measurement equation are jointly formulated to leverage all available information to achieve better performance. In the following, the state-space model of this system is presented.

### A. State Dynamics

The state vector of the tightly-coupled SLAM system at time step  $k$  is defined as

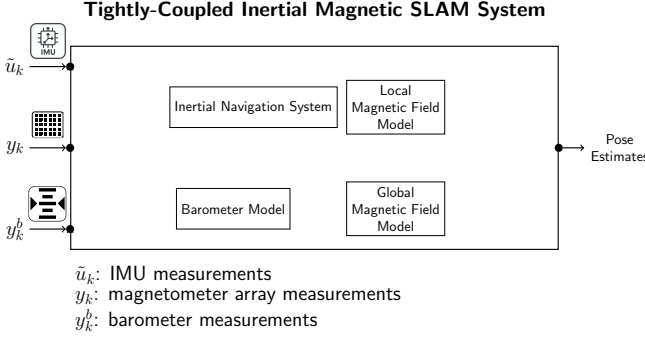
$$x_k \triangleq [p_k^\top \ v_k^\top \ q_k^\top \ b_{a,k}^\top \ b_{g,k}^\top \ \theta_k^\top \ \eta_k^\top]^\top \quad (20)$$

The state transition model is

$$x_{k+1} = f(x_k, \tilde{u}_k, w_k) \quad (21)$$

where

$$f(x_k, \tilde{u}_k, w_k) = \begin{bmatrix} f^{\text{ins}}(x_k^{\text{ins}}, \tilde{u}_k, w_k^{\text{ins}}) \\ f^\theta(\theta_k, x_k^{\text{ins}}, \tilde{u}_k, w_k^\theta) \\ \eta_k \end{bmatrix}. \quad (22)$$



$$\text{grad}(\theta_k) \triangleq \begin{bmatrix} 2\theta_k(8) & \theta_k(7) & \theta_k(6) \\ \theta_k(7) & 2\theta_k(5) & \theta_k(4) \\ \theta_k(6) & \theta_k(4) & -2(\theta_k(8) + \theta_k(5)) \end{bmatrix}. \quad (24b)$$

Here, the right-hand side of (24a) is more compact and computationally efficient than the left-hand side. Furthermore,  $\text{grad}(\theta_k) \in \mathbb{R}^{3 \times 3}$  has a clear physical interpretation, i.e., the gradient of the local magnetic field.

To sum up, there are two measurement equations for magnetometer array measurements: the equation used by the MAINS and the equation (23). They are used in an alternating manner: the former is employed at every update step except once  $D$  samples, when the second model is used instead. That is,

$$y_k = \begin{cases} h^m(x_k) + e_k & \text{for } k = D, 2D, \dots \\ [H^{\text{mains}} \ 0]x_k + e_k & \text{Otherwise} \end{cases} \quad (25)$$

Lastly, similar to what was done for the loosely coupled IM-SLAM system, the measurement equation is augmented when barometer measurements are available.

## B. Measurement Equations

Since the state vector includes both the local and global magnetic field model coefficients, the magnetometer array's measurements can be expressed in terms of both models. To achieve IM-SLAM, one can use the measurement equations in an alternating manner from either the MAINS or the magnetic field SLAM system. A natural choice is to use the computationally efficient measurement equation from the MAINS most of the time, while occasionally using the more complex measurement equation from the magnetic field SLAM system. In this way, the system can benefit from the low-drift inertial navigation provided by the MAINS while still leveraging the global consistency of the magnetic field SLAM system. In the proposed tightly-coupled IM-SLAM, the measurement equation of the global model, which is based on (18), is further simplified to reduce computational complexity. The basic idea is that the magnetic field at any sensor's location can be viewed as a superimposition of the magnetic field in the center of the array and some local magnetic field variation. This results in

$$y_k = h^m(x_k) + e_k \quad (23a)$$

where

$$h^m(x_k) = \begin{bmatrix} R_k^\top \nabla \Psi(p_k) \\ R_k^\top \nabla \Psi(p_k) \\ \vdots \\ R_k^\top \nabla \Psi(p_k) \end{bmatrix} \eta_k + \begin{bmatrix} \Phi(r^{(1)}) - \Phi(0) \\ \Phi(r^{(2)}) - \Phi(0) \\ \vdots \\ \Phi(r^{(N)}) - \Phi(0) \end{bmatrix} \theta_k. \quad (23b)$$

Here, the first term computes the magnetic field at the center of the magnetometer array by the approximated GP model, while the second term captures the local variations across the array modeled by the polynomial model. Note that for the first-degree polynomial model, the second term can also be rewritten as

$$(\Phi(r^{(i)}) - \Phi(0))\theta_k = \text{grad}(\theta_k)r^{(i)} \quad (24a)$$

To evaluate the performance of the proposed loosely-coupled and tightly-coupled IM-SLAM systems, we conducted experiments in an indoor environment using a custom-built sensor array, see Fig. 4. The sensor array is equipped with an IMU, a barometer, and an array of magnetometers.

In each experiment, a person carried the sensor array and started moving in a room equipped with a motion capture system for several tens of seconds. The person then walked out of the room and explored the surrounding area for several minutes before returning to the room. In total, three types of trajectories were recorded: a trajectory with long straight segments, a trajectory with square loops, and a trajectory with spiral upward segments (climbing a spiral staircase). The characteristics of the datasets are summarized in TABLE I.

The IMU and magnetometers were sampled at 100 Hz, while the barometer was sampled at 10 Hz. When available, the motion capture system provided ground truth poses at 100 Hz. In the loosely-coupled IM-SLAM system, the odometry data was internally computed at 5 Hz ( $K = 20$ ). In the tightly-coupled SLAM system, the magnetic field model switching time was set to 1 second ( $D = 100$ ), the length scale of the approximated GP model  $l_{\text{SE}}$  was set to 0.7 meters. More details about the parameter settings can be found in the code repository.

The standard error-state extended Kalman filter (EKF) is used in all systems for state estimation; interested reader are referred to [27] for details.

### A. Comparison with the MAINS

In the first experiment, the loosely-coupled and tightly-coupled IM-SLAM systems were compared with MAINS.

TABLE I  
INFORMATION ABOUT THE DATASETS

Data sequence	LC-1	LC-2	LC-3	C-1	C-2	C-3	SS-1	SS-2	SS-3
Trajectory duration <sup>*</sup> (s)	239	237	234.5	208	107	118	192	181	194
Trajectory duration <sup>†</sup> (s)	204.61	205.96	198.18	165.78	72.00	78.12	141.47	131.83	143.01
Average height (m)	0.84	0.93	0.80	1.14	1.04	1.02	2.29	2.39	2.17
Maximum height difference (m)	1.68	1.68	1.59	1.76	1.76	1.85	4.53	4.36	4.28
Maximum magnetic field strength difference <sup>‡</sup> ( $\mu$ T)	25.26	19.51	19.16	15.87	13.59	14.21	64.28	45.80	41.86

\* including the initial part of the trajectory in the motion capture area, † excluding the initial part of the trajectory in the motion capture area.

+ the difference between the maximum and minimum magnetic field strength measured by the magnetometer array during the trajectory.

LC: long corridor C: corridor SS: spiral staircase.

Note that MAINS was modified in the same way as in Section III-A to integrate barometer measurements.

All three systems used the pose from the motion capture system as additional measurements when the sensor array was in the room at the beginning of the trajectory. This is to stabilize the IMU bias estimates, which is important for good positioning performance. During the later parts of the trajectory, the systems relied solely on measurements from the onboard sensors for positioning.

Three examples of the trajectories estimated by the three systems are shown in Fig. 7, Fig. 8, and Fig. 9, respectively. The quantitative results are summarized in TABLE II and TABLE III, where the horizontal error, vertical error, and yaw error at the end of the trajectories are reported. The horizontal error is defined as the Euclidean distance between the estimated position and the ground truth position projected onto the horizontal plane, while the vertical error is defined as the absolute difference between the estimated altitude and the ground truth altitude. The yaw error is defined as the absolute difference between the estimated yaw angle and the ground truth yaw angle.

It can be seen from the figures that all systems can track the general shape of the trajectories. The noticeable difference between the tightly coupled IM-SLAM and other systems is that the estimated trajectories by the former have more jerky segments, which occur when the systems switch between the two measurement models; see (25). This phenomenon could be attributed to two different modeling of the magnetic field models: the model in the first row of (25) is parameterized with the position of the body frame in the navigation frame while the model in the second row is parameterized with the (local) positions of the magnetometers in the body frame. This implies that the former allows direct observation of the position while the latter does not [28]. The sudden jump observed on the estimated trajectory is a sign of gaining positional information when switching from the latter to the former model. Another observation is that the trajectories estimated by the SLAM systems during the long straight segments are more concentrated than those estimated by MAINS (see Fig. 7), which indicates that the SLAM systems can better mitigate the drift during these segments. Moreover, from TABLE II and TABLE III, it can be seen that the tightly-coupled IM-SLAM system outperforms both MAINS and the loosely-coupled IM-

TABLE II  
HORIZONTAL (VERTICAL) ERROR AT THE END OF THE TRAJECTORIES  
WITH A BAROMETER. UNIT: METER

	MAINS	IM-SLAM (L.) <sup>*</sup>	IM-SLAM (T.) <sup>†</sup>
Long corridor-1	3.53 (0.29)	9.20 (0.91)	0.90 (0.22)
Long corridor-2	2.28 (0.17)	5.23 (1.01)	1.51 (0.16)
Long corridor-3	1.25 (0.13)	2.44 (0.42)	1.08 (0.10)
Corridor-1	5.22 (0.14)	10.46 (0.27)	2.57 (0.14)
Corridor-2	1.93 (0.09)	1.03 (0.77)	1.93 (0.13)
Corridor-3	1.98 (0.03)	1.76 (0.10)	1.78 (0.05)
Spiral staircase-1	3.55 (0.02)	5.22 (0.26)	1.79 (0.00)
Spiral staircase-2	3.59 (0.17)	3.45 (0.12)	2.43 (0.16)
Spiral staircase-3	8.37 (0.20)	9.13 (0.84)	3.20 (0.21)

\*: loosely coupled IM-SLAM system †: tightly coupled IM-SLAM system

TABLE III  
YAW ERROR AT THE END OF THE TRAJECTORIES WITH A BAROMETER.  
UNIT: DEGREE

	MAINS	IM-SLAM (L.) <sup>*</sup>	IM-SLAM (T.) <sup>†</sup>
Long corridor-1	1.45	1.59	0.28
Long corridor-2	0.79	1.68	2.34
Long corridor-3	0.29	1.30	1.65
Corridor-1	2.02	2.85	1.77
Corridor-2	3.00	1.38	1.05
Corridor-3	2.19	1.57	0.52
Spiral staircase-1	2.32	1.06	1.83
Spiral staircase-2	0.64	2.35	1.40
Spiral staircase-3	1.58	2.49	0.52

\*: loosely coupled IM-SLAM system †: tightly coupled IM-SLAM system

SLAM system in most cases.

### B. Ablation Study on the Effect of Barometer and Inertial Sensor Quality

In the second part of the experiment, the effect of the barometric measurements and inertial sensor quality on the performance of the algorithms was investigated. For the first part, the barometer measurements were removed from all three systems, and the results are summarized in TABLE IV and TABLE V. Comparing TABLE IV with TABLE II, it can be seen that both the vertical error and horizontal error of all three systems increase slightly without the barometer measurements, but the overall performance remains unchanged. Furthermore, the yaw error of all three systems do not change significantly as seen from TABLE V. This indicates that the IM-SLAM systems are not heavily reliant on the barometer

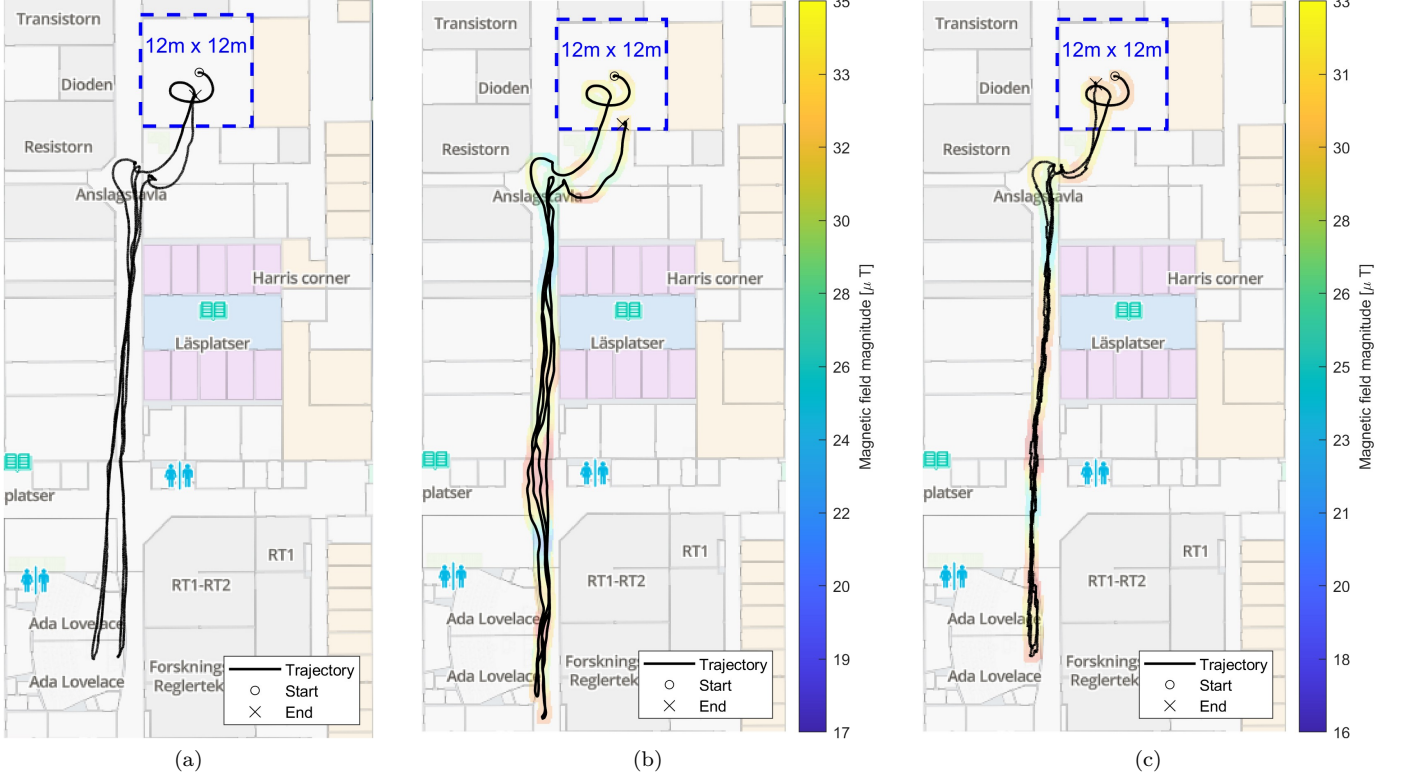


Fig. 7. Trajectories (Long corridor-2) estimated by (a) MAINS, (b) the loosely-coupled IM-SLAM system, and (c) the tightly-coupled IM-SLAM system. The room where the motion capture system is located is marked with a blue rectangle frame.

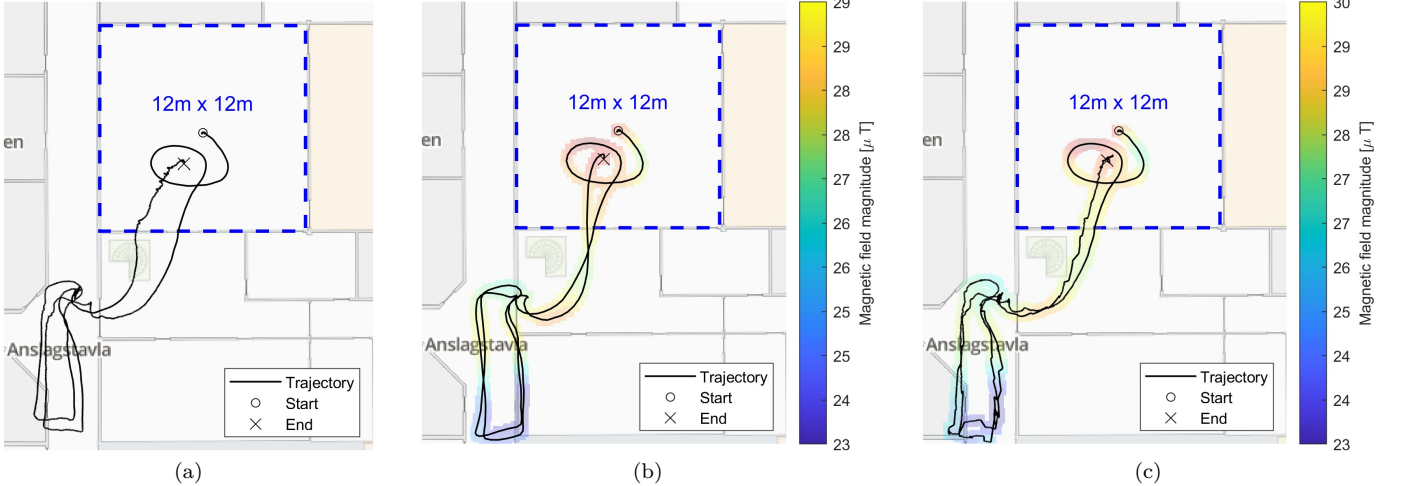


Fig. 8. Trajectories (Corridor-3) estimated by (a) MAINS, (b) the loosely-coupled IM-SLAM system, and (c) the tightly-coupled IM-SLAM system. The room where the motion capture system is located with a blue rectangle frame.

measurements. However, the barometer measurements are expected to have a more significant impact if explicit loop closure detection is to be performed in the SLAM systems, since the altitude information can help to distinguish different floors in a multi-floor building. For the second part, the IMU measurements quality is varied by averaging the measurements from different numbers of IMU sensors in Osmium MIMU 4844 IMU. The box plots of the horizontal errors at the end of the trajectories vs. the number of IMU sensors are shown in Fig. 10, 11, and 12.

It can be seen that the horizontal errors of the tightly-coupled IM-SLAM system are less sensitive to the number of IMU sensors compared to the other two systems, and it outperforms the other two algorithms on the datasets Long corridor and Corridor. On Spiral staircase datasets, the performance of the tightly-coupled IM-SLAM system improves as the number of IMU sensors increases, but it is not as good as MAINS when the number of IMU sensors is less than 4. We do not have a clear explanation for this phenomenon yet, but it could be related to the

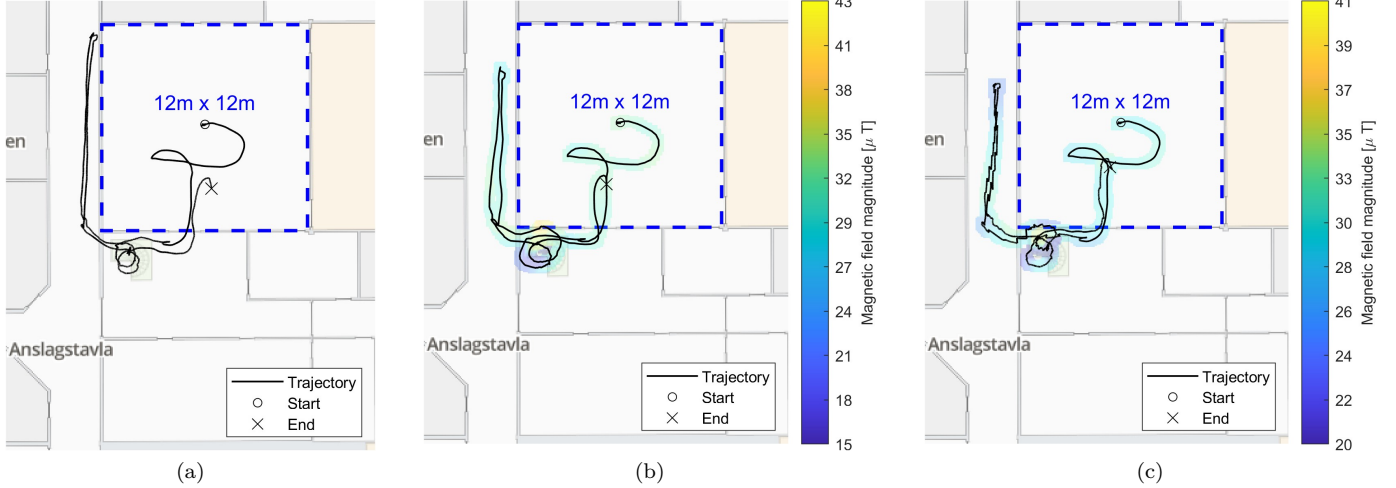


Fig. 9. Trajectories (Spiral staircase-2) estimated by (a) MAINS, (b) the loosely-coupled IM-SLAM system, and (c) the tightly-coupled IM-SLAM system. The room where the motion capture system is located is marked with a blue rectangle frame.

TABLE IV  
HORIZONTAL (VERTICAL) ERROR AT THE END OF THE TRAJECTORIES  
WITHOUT A BAROMETER. UNIT: METER

	MAINS	IM-SLAM (L.)*	IM-SLAM (T.)†
Long corridor-1	3.80 (1.01)	6.84 (6.75)	0.97 (0.83)
Long corridor-2	2.33 (1.16)	8.41 (1.21)	1.49 (0.11)
Long corridor-3	1.19 (1.21)	4.30 (0.89)	1.23 (0.43)
Corridor-1	5.35 (0.54)	11.05 (0.36)	2.45 (0.28)
Corridor-2	1.82 (0.44)	0.99 (0.95)	1.76 (0.32)
Corridor-3	2.02 (0.52)	1.80 (0.36)	1.89 (0.51)
Spiral staircase-1	3.00 (0.41)	6.90 (1.08)	1.74 (0.16)
Spiral staircase-2	3.39 (0.10)	4.33 (0.90)	2.51 (0.22)
Spiral staircase-3	8.22 (0.65)	8.48 (2.14)	4.13 (0.91)

\*: loosely coupled IM-SLAM system †: tightly coupled IM-SLAM system

TABLE V  
YAW ERROR AT THE END OF THE TRAJECTORIES WITHOUT A  
BAROMETER. UNIT: DEGREE

	MAINS	IM-SLAM (L.)*	IM-SLAM (T.)†
Long corridor-1	0.87	2.85	0.29
Long corridor-2	1.24	2.17	2.31
Long corridor-3	0.23	1.76	2.00
Corridor-1	2.11	3.12	1.32
Corridor-2	2.90	1.37	0.90
Corridor-3	2.11	1.60	0.28
Spiral staircase-1	2.25	0.23	1.62
Spiral staircase-2	0.56	2.20	0.80
Spiral staircase-3	1.71	0.41	1.40

\*: loosely coupled IM-SLAM system †: tightly coupled IM-SLAM system

fact that the datasets Spiral staircase have more dynamic motions (e.g., turning and climbing) than the other two types of datasets. Further investigation is needed to fully understand this phenomenon. Lastly, the sudden increase in horizontal error when using 32 IMU sensors is due to exceptionally worse performance on one of the datasets (Spiral staircase-3), which is currently under investigation.

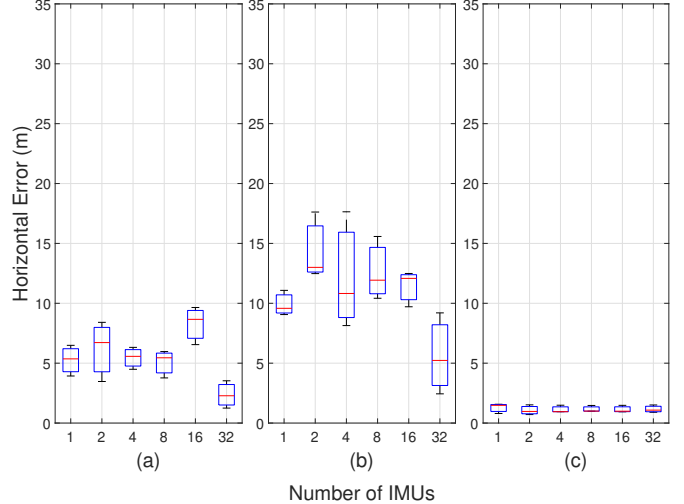


Fig. 10. Box plot of horizontal errors (red: median) at the end of trajectories of all algorithms using different numbers of IMU sensors on the Long corridor datasets. The algorithms from left to right are (a) MAINS, (b) the loosely-coupled IM-SLAM system, and (c) the tightly-coupled IM-SLAM system.

## VII. CONCLUSION

In this paper, a loosely coupled and a tightly coupled IM-SLAM system were proposed. Both systems rely solely on commonly available low-cost sensors: an inertial measurement unit (IMU), a magnetometer array, and a barometer. The proposed systems have position errors on the order of meters per 100 meters traveled, which showcases the feasibility of developing magnetic field-based SLAM systems with low-cost sensors. Experimental results demonstrate that the tightly coupled IM-SLAM system achieves better performance than the loosely coupled counterpart. This improvement arises because the tightly coupled system integrates the local and global magnetic field model within a unified framework, rather than employing them in a two-stage manner as in the loosely

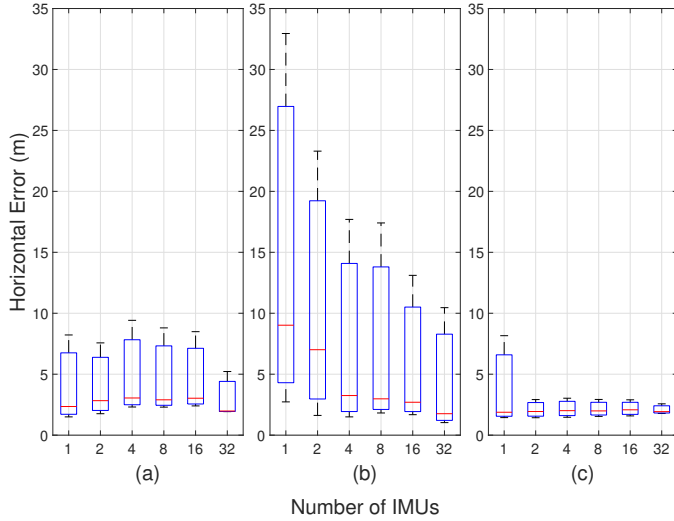


Fig. 11. Box plot of horizontal errors (red: median) at the end of trajectories of all algorithms using different numbers of IMU sensors on the Corridor datasets. The algorithms from left to right are (a) MAINS, (b) the loosely-coupled IM-SLAM system, and (c) the tightly-coupled IM-SLAM system.

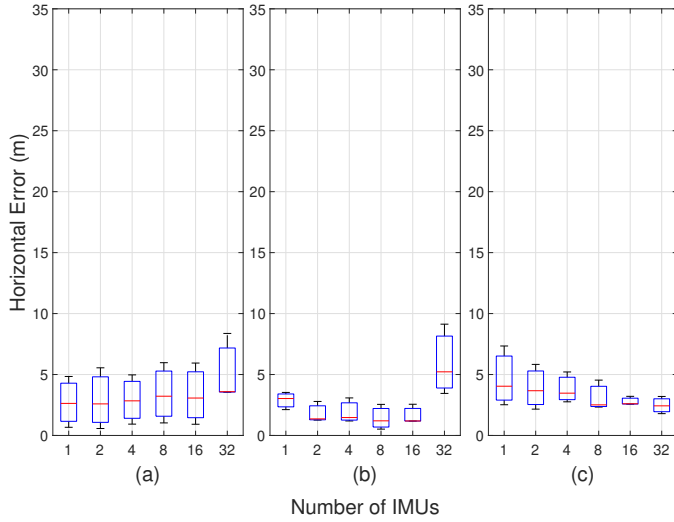


Fig. 12. Box plot of horizontal errors (red: median) at the end of trajectories of all algorithms using different numbers of IMU sensors on the Spiral staircase datasets. The algorithms from left to right are (a) MAINS, (b) the loosely-coupled IM-SLAM system, and (c) the tightly-coupled IM-SLAM system.

coupled design. Furthermore, the experiments show that incorporating a barometer primarily benefits IM-SLAM performance in the vertical direction, and that the IMU quality can be degraded by approximately a factor of 32 without substantially affecting the overall accuracy. These results demonstrate the potential of applying the proposed systems in emergency response scenarios such as mine/fire rescue.

## REFERENCES

- R. Mur-Artal, J. M. M. Montiel, and J. D. Tardós, “ORB-SLAM: A versatile and accurate monocular slam system,” *IEEE Trans. Robot.*, vol. 31, no. 5, pp. 1147–1163, 2015.
- W. Hess, D. Kohler, H. Rapp, and D. Andor, “Real-time loop closure in 2d LIDAR SLAM,” in Proc. 2016 IEEE Int. Conf. Robot. Autom. (ICRA), Stockholm, Sweden, May 2016, pp. 1271–1278.
- S. Park, T. Schöps, and M. Pollefeys, “Illumination change robustness in direct visual SLAM,” in Proc. 2017 IEEE Int. Conf. Robot. Autom. (ICRA), Marina Bay Sands, Singapore, May 2017, pp. 4523–4530.
- Q. Zou, Q. Sun, L. Chen, B. Nie, and Q. Li, “A comparative analysis of LiDAR SLAM-based indoor navigation for autonomous vehicles,” *IEEE Trans. Intell. Transp. Syst.*, vol. 23, no. 7, pp. 6907–6921, 2022.
- B. Li, T. Gallagher, A. G. Dempster, and C. Rizos, “How feasible is the use of magnetic field alone for indoor positioning?” in Proc. 2012 Int. Conf. Indoor Position. Indoor Navig. (IPIN), Sydney, Australia, Nov 2012, pp. 1–9.
- M. Kok and A. Solin, “Scalable magnetic field SLAM in 3D using gaussian process maps,” in Proc. 2018 21st Int. Conf. Inf. Fusion (FUSION), Cambridge, United Kingdom, July 2018, pp. 1353–1360.
- F. Viset, R. Helmons, and M. Kok, “An extended Kalman filter for magnetic field SLAM using Gaussian process regression,” *Sensors*, vol. 22, no. 8, 2022.
- I. Vallivaara, J. Haverinen, A. Kemppainen, and J. Röning, “Magnetic field-based SLAM method for solving the localization problem in mobile robot floor-cleaning task,” in Proc. 2011 15th Int. Conf. Adv. Robot. (ICAR), Montevideo, Uruguay, June 2011, pp. 198–203.
- N. Pavlasek, C. C. Cossette, D. Roy-Guay, and J. R. Forbes, “Magnetic navigation using attitude-invariant magnetic field information for loop closure detection,” in Proc. 2023 IEEE/RSJ Int. Conf. Intell. Robots Syst. (IROS), Detroit, USA, 2023, pp. 5251–5257.
- I. Vallivaara, Y. Dong, and T. Arslan, “Saying goodbyes to rotating your phone: Magnetometer calibration during SLAM,” in Proc. 2024 14th Int. Conf. Indoor Position. Indoor Navig. (IPIN), Hong Kong, China, Oct 2024, pp. 1–7.
- C. Huang, G. Hendeby, H. Fourati, C. Prieur, and I. Skog, “MAINS: A magnetic-field-aided inertial navigation system for indoor positioning,” *IEEE Sens. J.*, vol. 24, no. 9, pp. 15156–15166, 2024.
- E. Prigge and J. How, “Signal architecture for a distributed magnetic local positioning system,” *IEEE Sens. J.*, vol. 4, no. 6, pp. 864–873, 2004.
- R. Wang, R. Tan, Z. Yan, and C. X. Lu, “Orientation-aware 3d SLAM in alternating magnetic field from powerlines,” *Proc. ACM Interact. Mob. Wearable Ubiquitous Technol.*, vol. 7, no. 4, Jan. 2024.
- H. Shen, Z. Wu, W. Wang, Q. Lyu, H. Zhou, and D. Wang, “IDF-MFL: Infrastructure-free and drift-free magnetic field localization for mobile robot,” in Proc. 2024 IEEE/RSJ Int. Conf. Intell. Robots Syst. (IROS), Abu Dhabi, UAE, October 2024, pp. 2278–2285.
- T. Zhang, L. Wei, J. Kuang, H. Tang, and X. Niu, “Magodo: Motion speed estimation for indoor robots based on dual magnetometers,” *Measurement*, vol. 222, p. 113688, 2023.
- Y. Wang, J. Kuang, T. Liu, X. Niu, and J. Liu, “Crowdmagmap: Crowdsourcing-based magnetic map construction for shopping mall,” *IEEE Internet Things J.*, vol. 11, no. 3, pp. 5362–5373, 2024.
- J. Kuang, Y. Wang, L. Ding, B. Zhou, L. Xu, L. Cao, L. He, Y. Wen, and X. Niu, “Crowdmagmap 2.0: Crowdsourced magnetic mapping for multi-floor underground parking lot navigation,” *IEEE Trans. Intell. Transp. Syst.*, pp. 1–14, 2025.
- M. Kok and A. Solin, “Online one-dimensional magnetic field SLAM with loop-closure detection,” in Proc. 2024 IEEE Int. Conf. Multisensor Fusion Integr. Intell. Syst. (MFI), Pilsen, Czechia, Sep. 2024, pp. 1–7.
- S. Chen, J. Kuang, Y. Wang, T. Wang, and X. Niu, “A pedestrian positioning method for urban canyon environments using magnetic field matching/inertial odometry fusion,” *IEEE Trans. Instrum. Meas.*, vol. 74, pp. 1–15, 2025.
- I. Skog, G. Hendeby, and F. Gustafsson, “Magnetic odometry – a model-based approach using a sensor array,” in Proc. Int. Conf. Inf. Fusion (FUSION), Cambridge, United Kingdom, July 2018, pp. 794–798.

- [21] I. Skog, G. Hendeby, and F. Trulsson, "Magnetic-field based odometry – an optical flow inspired approach," in Proc. Int. Conf. Indoor Position. Indoor Navig. (IPIN), Lloret de Mar, Spain, Nov. 2021, pp. 1–8.
- [22] M. Zmitri, H. Fourati, and C. Prieur, "Magnetic Field Gradient-Based EKF for Velocity Estimation in Indoor Navigation," Sensors, vol. 20, no. 20, p. 5726, 2020.
- [23] A. Solin, M. Kok, N. Wahlström, T. B. Schön, and S. Särkkä, "Modeling and interpolation of the ambient magnetic field by Gaussian processes," IEEE Trans. Robot., vol. 34, no. 4, pp. 1112–1127, 2018.
- [24] F. Viset, J. T. Gravdahl, and M. Kok, "Magnetic field norm SLAM using Gaussian process regression in foot-mounted sensors," in Proc. Eur. Control Conf. (ECC), Rotterdam, Netherlands, June 2021, pp. 392–398.
- [25] J. D. Jackson, Classical electrodynamics. John Wiley & Sons, 2021, vol. 2.
- [26] C. K. Williams and C. E. Rasmussen, Gaussian processes for machine learning. MIT press Cambridge, MA, 2006, vol. 2.
- [27] J. Solà, "Quaternion kinematics for the error-state Kalman filter," arXiv preprint arXiv:1711.02508, vol. abs/1711.02508, 2017. [Online]. Available: <http://arxiv.org/abs/1711.02508>
- [28] C. Huang, G. Hendeby, and I. Skog, "An observability-constrained magnetic field-aided inertial navigation system," in Proc. 2024 14th Int. Conf. Indoor Position. Indoor Navig. (IPIN), Hong Kong, China, Oct. 2024, pp. 1–6.



**Isaac Skog** (Senior Member, IEEE) received the B.Sc. and M.Sc. degrees in electrical engineering from the KTH Royal Institute of Technology, Stockholm, Sweden, in 2003 and 2005, respectively. In 2010, he received the Ph.D. degree in signal processing with a thesis on low-cost navigation systems.

In 2009, he spent 5 months with the Mobile Multi-Sensor System Research Team, University of Calgary, Calgary, AB, Canada, as a Visiting Scholar and in 2011 he spent 4 months with the Indian Institute of Science, Bangalore, India, as a Visiting Scholar. Between 2010 and 2017, he was a Researcher with the KTH Royal Institute of Technology. He is currently an Associate Professor with Linköping University, Linköping, Sweden, and a Senior Researcher with Swedish Defence Research Agency (FOI), Stockholm, Sweden. He is the author and coauthor of more than 60 international journal and conference publications. He was the recipient of the Best Survey Paper Award by the IEEE Intelligent Transportation Systems Society in 2013.



**Chuan Huang** (Student member, IEEE) received the B.Sc. from Beihang University in 2018 and the M.Sc. degree from China Electronics Technology Group Corporation Academy of Electronics and Information Technology in 2021. From 2021 to 2014, he studied at Linköping University, Sweden, and he is now a PhD student at the KTH Royal Institute of Technology, Stockholm, Sweden.

His main research interest is magnetic field-based positioning and sensor calibration.



**Gustaf Hendeby** (Senior member, IEEE) received the M.Sc. degree in applied physics and electrical engineering in 2002 and the Ph.D. degree in automatic control in 2008, both from Linköping University, Linköping, Sweden. He is Associate Professor and Docent in the division of Automatic Control, Department of Electrical Engineering, Linköping University.

He worked as Senior Researcher at the German Research Center for Artificial Intelligence (DFKI) 2009–2011, and Senior Scientist at Swedish Defense Research Agency (FOI) and held an adjunct Associate Professor position at Linköping University 2011–2015. His main research interests are stochastic signal processing and sensor fusion with applications to nonlinear problems, target tracking, and simultaneous localization and mapping (SLAM), and is the author of several published articles and conference papers in the area. He has experience of both theoretical analysis as well as implementation aspects. Dr. Hendeby was an Associate Editor for IEEE Transactions on Aerospace and Electronic Systems in the area of Target Tracking and Multisensor Systems 2018–2025, and is since 2025 a Senior Editor. In 2022 he served as general chair for the 25th IEEE International Conference on Information Fusion (FUSION) in Linköping, Sweden.